

A Novel 3D Non-Stationary GBSM for 6G THz Ultra-Massive MIMO Wireless Systems

Jun Wang, *Student Member, IEEE*, Cheng-Xiang Wang [✉], *Fellow, IEEE*, Jie Huang [✉], *Member, IEEE*, Haiming Wang [✉], *Member, IEEE*, Xiqi Gao [✉], *Fellow, IEEE*, Xiaohu You [✉], *Fellow, IEEE*, and Yang Hao [✉], *Fellow, IEEE*

I. INTRODUCTION

Abstract—Terahertz (THz) communication is now being considered as one of possible technologies for the sixth generation (6G) wireless communication systems. In this paper, a novel three-dimensional (3D) space-time-frequency non-stationary theoretical channel model is first proposed for 6G THz wireless communication systems employing ultra-massive multiple-input multiple-output (MIMO) technologies with long traveling paths. Considering frequency-dependent diffuse scattering, which is a special property of THz channels different from millimeter wave (mmWave) channels, the relative angles and delays of rays within one cluster will evolve in the frequency domain. Then, a corresponding simulation model is proposed with discrete angles calculated using the method of equal area (MEA). The statistical properties of the proposed theoretical and simulation models are derived and compared, showing good agreements. The accuracy and flexibility of the proposed simulation model are demonstrated by comparing the simulation results of the relative angle spread and root mean square (RMS) delay spread with corresponding measurements.

Index Terms—6G, THz GBSM, ultra-massive MIMO, long traveling paths, space-time-frequency non-stationarity.

Manuscript received May 18, 2020; revised November 20, 2020 and March 22, 2021; accepted June 1, 2021. Date of publication October 1, 2021; date of current version December 17, 2021. This work was supported in part by the National Key R&D Program of China under Grant 2018YFB1801101, in part by the National Natural Science Foundation of China (NSFC) under Grants 61960206006 and 61901109, in part by the Frontiers Science Center for Mobile Information Communication, and Security, the High Level Innovation and Entrepreneurial Research Team Program in Jiangsu, the High Level Innovation and Entrepreneurial Talent Introduction Program in Jiangsu, the Research Fund of National Mobile Communications Research Laboratory, Southeast University, under Grants 2020B01 and 2021B02, in part by the Fundamental Research Funds for the Central Universities under Grant 2242021R30001, and in part by the EU H2020 RISE TESTBED2 project under Grant 872172. The review of this article was coordinated by Prof. Thomas Kurner. (*Corresponding author: Cheng-Xiang Wang.*)

Jun Wang, Cheng-Xiang Wang, Jie Huang, Xiqi Gao, and Xiaohu You are with the National Mobile Communications Research Laboratory, School of Information Science and Engineering, Southeast University, Nanjing 210096, China, and also with the Purple Mountain Laboratories, Nanjing 211111, China (e-mail: jun.wang@seu.edu.cn; chxwang@seu.edu.cn; j_huang@seu.edu.cn; xqgao@seu.edu.cn; xhyu@seu.edu.cn).

Haiming Wang is with the State Key Laboratory of Millimeter Wave, School of Information Science and Engineering, Southeast University, Nanjing 210096, China, and also with the Purple Mountain Laboratories, Nanjing 211111, China (e-mail: hmwang@seu.edu.cn).

Yang Hao is with the School of Electronic Engineering and Computer Science, Queen Mary University of London, London E1 4NS, U.K. (e-mail: y.hao@qmul.ac.uk).

Digital Object Identifier 10.1109/TVT.2021.3117239

THE peak data rate and connection density of the fifth generation (5G) wireless communication system are 20 gigabits per second (Gbps) and 10^6 devices/km², respectively [1]. It is expected that the sixth generation (6G) wireless system will reach terabits per second (Tbps) level in terms of the peak data rate and 10^7 – 10^8 devices/km² in terms of connection density [2]–[4]. To meet the massive data flow and massive connectivity requirements in 6G, increasing transmission bandwidth and improving spectrum efficiency are potential solutions. Terahertz (THz) communication has the ability to provide more than one hundred gigahertz (GHz) bandwidth [5] and can theoretically achieve ultra-high transmission rate of 100 Gbps or even higher [6]. By filling the gap between millimeter wave (mmWave) and optical wireless communication bands, THz communication has attracted great interests worldwide and been considered as one of the most promising 6G technologies. It has plenty of promising applications such as data center [7], [8] and kiosk downloading [9], [10], which support short-range (about 1 m) communications between fixed devices and terminal equipment such as smart phones. THz communications can also be applied to smart rail systems [11]–[13] by providing high data rate transmissions for passengers. In addition, the small size of THz devices makes nanoscale communications possible such as chip-to-chip [14], [15], computer motherboard links [16], and intra-body communications [17]–[20].

THz channel models that can accurately reflect THz channel characteristics are prerequisite for the design, optimization, and performance evaluation of THz wireless communication systems. The investigation of channel characteristics is very important for accurate channel modeling. Due to the high frequency and large bandwidth of THz communications, propagation mechanisms of THz bands are quite different from those of lower frequency bands such as mmWave bands. The THz propagation mechanisms were studied in [21]–[27]. In [21] and [22], THz measurements and modeling of multiple reflection effects in different materials were introduced. The reflection loss showed great dependence on frequency and materials and could be calculated by Kirchhoff theory. According to the measurement in [23], high-order paths were very hard to be detected due to high reflection loss which means that the number of multipaths is limited. The diffusely scattered propagation was investigated in [24]–[28]. In [24], the detected signal powers in all directions

for different materials were measured and simulated. Frequency-dependent scattering was also measured and simulated in [25] and [26]. The wavelength of THz waves is comparable to the roughness of some common materials. As a result, more power is diffusely scattered when frequency increases. Most of the diffusely scattered rays surround the specular reflected paths. In this case, scattered rays far away from the specular reflection points can be neglected [27].

Apart from investigations on THz channel characteristics, a number of THz channel models were proposed for THz communication systems. In [29], a multi-ray ray tracing channel model for THz indoor communication was presented and validated with experiments. In [30], a three-dimensional (3D) time-variant THz channel model based on ray tracing was investigated for dynamic environments. However, channel models based on ray tracing methods are not general and flexible. In [31], a stochastic THz indoor channel model considering the frequency dispersion was presented and verified by ray tracing. In [32], the authors investigated root mean square (RMS) delay spread and angular spread that were modeled by second order polynomial parameters for THz indoor communications. However, the existing stochastic THz channel models cannot show the unique propagation characteristics of THz bands such as frequency-dependent scattering.

In the existing THz channel models, massive multiple-input multiple-output (MIMO) were rarely mentioned. However, in THz communication systems, ultra-massive MIMO technologies employing hundreds or even thousands of antennas are considered as one of the solutions to compensate the high path loss [33] and are expected to be utilized in 6G [3], [4]. Massive MIMO channel models and measurements considering spatial non-stationarity were studied in [34]–[39]. In [34], massive MIMO channel measurements and models were summarized. In [40]–[42], channel measurements for massive MIMO channels in different scenarios at mmWave were presented. A novel 3D geometric-based stochastic model (GBSM) based on homogeneous Poisson point process was proposed for mmWave channels [42]. A GBSM for mobile-to-mobile scenarios for mmWave bands was presented in [43]. However, the existing massive MIMO channel models have only considered characteristics of sub-6GHz and mmWave bands, and are not suitable for THz communication systems because propagation mechanisms in THz bands are quite different from those of lower frequencies.

In addition, time variant channels caused by long traveling paths also need to be characterized in THz communication systems. It should be noted that for a realistic application of THz communications, the range of movement is not necessarily very long. For example, in some typical application scenarios such as movement of human body, even a short traveling path of several meters is quite long compared with the wavelength of THz signals. Unlike high mobility scenarios such as high-speed train and vehicle-to-vehicle communications in fifth generation (5G) systems, THz communications are usually applied in relatively static environments. The non-stationarity in the time domain is caused by the continuous moving of the transmitter or receiver over a long distance.

To the best of the authors knowledge, stochastic space-time-frequency non-stationary GBSMs for massive MIMO THz channels are still missing in the literature. We have done some early investigations in [44], [45]. However, the simulation models of THz channels were not studied in [45]. The major contributions and novelties of this paper are listed as follows.

- 1) A novel theoretical space-time-frequency non-stationary GBSM for ultra-massive MIMO THz channels considering long traveling paths is first proposed. The non-stationarity in space, time, and frequency domains caused by ultra-massive MIMO, long traveling paths, and large bandwidths, respectively, are considered.
- 2) The statistical properties of the theoretical model such as space-time-frequency correlation function (STFCF), time autocorrelation function (ACF), spatial cross-correlation function (CCF), and frequency correlation function (FCF) are derived.
- 3) The corresponding simulation model with discrete angles generated by the method of equal area (MEA) is then proposed. Its statistical properties are derived, verified by simulation results, and compared with those of the theoretical model, showing good agreements. Some simulated statistical properties are also compared with corresponding measurements, illustrating the validity and flexibility of the proposed THz simulation model.

The remainder of this paper is organized as follows. In Section II, the proposed theoretical THz GBSM is described in detail and the channel impulse response (CIR) is presented. In Section III, statistical properties of the theoretical THz channel model are derived. Then, the corresponding simulation model is proposed with discrete angles calculated using the MEA and its statistical properties are derived in Section IV. In Section V, statistical properties of the theoretical model and simulation model, simulation results, and measurements are compared and discussed. Finally, conclusions are drawn in Section VI.

II. A 3D THZ NON-STATIONARY THEORETICAL MODEL

A. Description of the Channel Model

In this sub-section, a 3D non-stationary THz massive MIMO channel model is proposed. The proposed model is illustrated in Fig. 1. Both transmitted antennas (Tx) and received antennas (Rx) are equipped with a massive number of antenna elements. To simplify the calculation, uniform linear arrays (ULAs) are assumed in this model. We assume that Tx has N_T antenna elements with the same distance δ_T . It should be noted that only propagation model is studied so that each element in the array is assumed omni-directional. The direction of the Tx is represented by the elevation and azimuth angles β^T and α^T , respectively. Rx is represented similarly. The p th transmit and q th receive antenna element are denoted by A_p^T and A_q^R , respectively. The position vector of the A_p^T from the center of the transmitted array $\vec{\delta}_p$ and A_q^R from the center of the received array $\vec{\delta}_q$ are expressed by

$$\vec{\delta}_p = \delta_p \cdot \begin{bmatrix} \cos \beta^T \cos \alpha^T \\ \cos \beta^T \sin \alpha^T \\ \sin \beta^T \end{bmatrix} \quad (1)$$

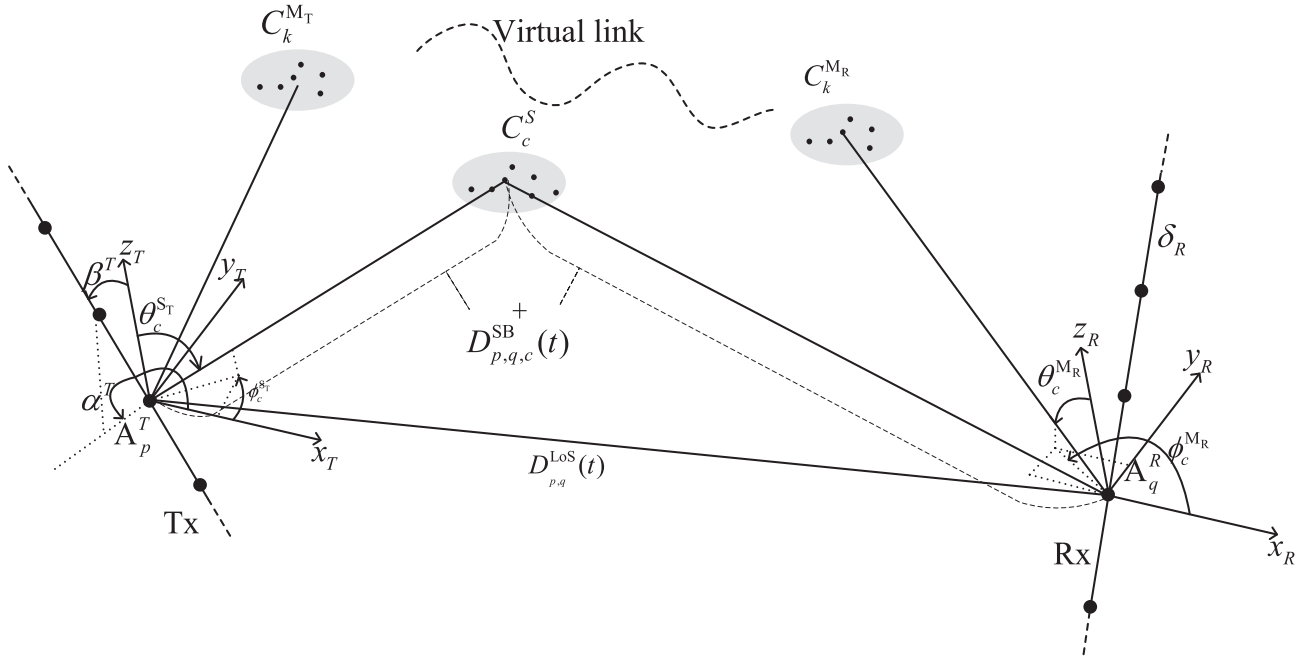


Fig. 1. A 3D THz GBSM for massive MIMO communication systems.

TABLE I
DEFINITIONS OF MAIN PARAMETERS FOR THE PROPOSED THZ MASSIVE MIMO CHANNEL MODEL

Parameters	Definitions
δ_T, δ_R	Distances between consecutive elements in the Tx and Rx array, respectively
D	Distance between the center of Tx and Rx
$D_{p,q}^{LoS}(t)$	Distance from A_p^T to A_q^R
$D_{p,q,c}^{SB}(t)$	Total distance of the path: $A_p^T - C_c^S - A_q^R$
$D_{p,q,c,l}^{SB}(t, f_i)$	Total distance of the path: $A_p^T - C_{c,l}^S - A_q^R$
$D_{p,q,k}^{MB}(t)$	Total distance of the path: $A_p^T - C_k^{MT} - C_k^{MR} - A_q^R$ +
$D_{p,q,k,m}^{MB}(t)$	Total distance of the path: $A_p^T - C_{k,m}^{MT} - C_{k,m}^{MR} - A_q^R$
$\beta^{T(R)}, \alpha^{T(R)}$	Elevation and azimuth angles of the Tx(Rx) array, respectively
θ^{LoS}, ϕ^{LoS}	Elevation and azimuth angles of the Rx with respect to the Tx, respectively
$\theta_{p(q),c}^{ST(R)}(t), \phi_{p(q),c}^{ST(R)}(t)$	Elevation and azimuth angles of $C_c^{ST(R)}$, respectively
$\theta_{p(q),c,l}^{ST(R)}(t, f_i), \phi_{p(q),c,l}^{ST(R)}(t, f_i)$	Elevation and azimuth angles of the scatterer $C_{c,l}^{ST(R)}$, respectively
$\theta_{p(q),k}^{MT(R)}(t), \phi_{p(q),k}^{MT(R)}(t)$	Elevation and azimuth angles of $C_k^{MT(R)}$, respectively
$\theta_{p(q),k,m}^{MT(R)}(t, f_i), \phi_{p(q),k,m}^{MT(R)}(t, f_i)$	Elevation and azimuth angles of the scatterer $C_{k,m}^{ST(R)}$, respectively
ζ^R, ξ^R	Elevation and azimuth angles of the velocity of the Rx, respectively

$$\vec{\delta}_q = \delta_q \cdot \begin{bmatrix} \cos \beta^R \cos \alpha^R \\ \cos \beta^R \sin \alpha^R \\ \sin \beta^R \end{bmatrix} \quad (2)$$

with $\delta_p = \frac{N_T - 2p + 1}{2} \delta_T$ and $\delta_q = \frac{N_R - 2q + 1}{2} \delta_R$. In addition, the speed of Rx is denoted by v^R . The elevation and azimuth angles of the speed are represented by ζ^R and ξ^R , respectively.

The concept of cluster is proposed [46] to simplify the analysis of multipaths. In THz band, the wavelength of the carrier frequency is less than one millimeter and comparable to the surface roughness of some common objects such as furniture and walls. In this model, each cluster is comprised of diffusely scattering rays from the rough surface. The center of cluster is considered

as the specular reflected point. According to the study in [24], the power and angle of these clusters are frequency-dependent.

The received signal at the Rx is composed of the line of sight (LoS), C_S single-bounce clusters (SBCs), and C_M multi-bounce clusters (MBCs). In the picture, only the c th SBC and k th MBC are represented for clarity. Each MBC consists of two clusters at both Tx and Rx connected by a virtual link. For the k th MBC the transmit-side and receive-side MBC are denoted as C_k^{MT} and C_k^{MR} , respectively. The c th SBC is denoted by C_c^S . Both SBCs and MBCs are comprised of infinite scatterers. The main parameters are defined in Table I.

Considering the frequency domain non-stationarity in the propagation channel, the whole band is divided into N_F small sub-bands in which the channel is considered stationary in

frequency domain [29]. The CIR of sub-band $h_{p,q}(t, \tau, f_i)$ is represented as

$$h_{p,q}(t, \tau, f_i) = h_{p,q}^{\text{LoS}}(t, \tau, f_i) + \sum_{c=1}^{C_{\text{SB}}} h_{p,q,c}^{\text{SB}}(t, \tau, f_i) + \sum_{k=1}^{C_{\text{MB}}} h_{p,q,k}^{\text{MB}}(t, \tau, f_i) \quad (3)$$

where LoS, SB, and MB refer to line of sight, single bounce, and multi bounce components, respectively. In (3), the LoS component is represented as

$$h_{p,q}^{\text{LoS}}(t, \tau, f_i) = \sqrt{\frac{K}{K+1}} \times e^{-j(2\pi f_i \tau_{p,q}^{\text{LoS}}(t))} \delta(\tau - \tau_{p,q}^{\text{LoS}}(t)) \quad (4)$$

where K is the Rician factor. The delay $\tau_{p,q}^{\text{LoS}}(t)$ is given by $D_{p,q}^{\text{LoS}}(t)/c_0$ where c_0 refers to the speed of light. The distance between A_p^T and A_q^R is calculated by the vector $\vec{D}_{p,q}^{\text{LoS}}(t) = \|\vec{D}_{p,q}^{\text{LoS}}(t)\|$ where $\|\cdot\|$ calculates the Frobenius norm. The $\vec{D}_{p,q}^{\text{LoS}}(t)$ is expressed as

$$\vec{D}_{p,q}^{\text{LoS}}(t) = \vec{D} + \vec{\delta}_q - \vec{\delta}_p + \vec{v}^R \cdot t \quad (5)$$

where

$$\vec{D} = D \cdot \begin{bmatrix} \cos \theta^{\text{LoS}} \cos \phi^{\text{LoS}} \\ \cos \theta^{\text{LoS}} \sin \phi^{\text{LoS}} \\ \sin \theta^{\text{LoS}} \end{bmatrix} \quad (6)$$

$$\vec{v}^R = v^R \begin{bmatrix} \cos \zeta^R \cos \xi^R \\ \cos \zeta^R \sin \xi^R \\ \sin \zeta^R \end{bmatrix}. \quad (7)$$

The SB components and the MB components can be expressed as

$$h_{p,q,c}^{\text{SB}}(t, \tau, f_i) = \sqrt{\frac{1}{K+1}} \lim_{L_c \rightarrow \infty} \sum_{l=1}^{L_c} \sqrt{\frac{P_c^{\text{SB}}}{L_c}} e^{-j(2\pi f_i \tau_{p,q,c,l}^{\text{SB}}(t) - \Theta_{c,l}^{\text{SB}})} \delta(\tau - \tau_{p,q,c,l}^{\text{SB}}(t)) \quad (8)$$

$$h_{p,q,k}^{\text{MB}}(t, \tau, f_i) = \sqrt{\frac{1}{K+1}} \lim_{M_k \rightarrow \infty} \sum_{m=1}^{M_k} \sqrt{\frac{P_k^{\text{MB}}}{M_k}} e^{-j(2\pi f_i \tau_{p,q,k,m}^{\text{MB}}(t) - \Theta_{k,m}^{\text{MB}})} \delta(\tau - \tau_{p,q,k,m}^{\text{MB}}(t)) \quad (9)$$

where $\Theta_{c,l}^{\text{SB}}$ and $\Theta_{k,m}^{\text{MB}}$ are uniformly distributed over $(0, 2\pi)$. The L_c and M_k refer to the number of rays for the c th single-bounce cluster and the k th multi-bounce cluster, respectively. In addition, P_c^{SB} and P_k^{MB} are the frequency-dependent power of corresponding clusters. The symbols $\tau_{p,q,c,l}^{\text{SB}}(t)$ and $\tau_{p,q,k,m}^{\text{MB}}(t)$ are the delays of corresponding rays.

The delay $\tau_{p,q,c,l}^{\text{SB}}(t)$ of the l th ray in the c th SBC is composed of two parts, i.e.,

$$\tau_{p,q,c,l}^{\text{SB}}(t) = \tau_{p,q,c}^{\text{SB}}(t) + \Delta\tau_{p,q,c,l}^{\text{SB}}(t) \quad (10)$$

where $\tau_{p,q,c}^{\text{SB}}(t)$ is the delay of the path $A_p^T - C_c^S - A_q^R$. Here, C_c^S represents the center of the cluster so this path is the specular

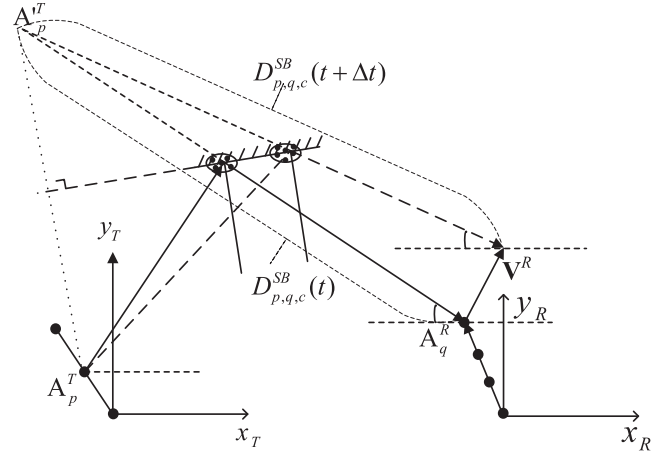


Fig. 2. Geometric relationship of the time-variant path via the SBC.

reflection path of this cluster. The relative delay with respect to this specular reflection path is denoted by $\Delta\tau_{p,q,c,l}^{\text{SB}}(t)$.

To obtain the $\Delta\tau_{p,q,c,l}^{\text{SB}}(t)$, we need to generate the initial delay between the center of Tx and Rx arrays via all the clusters at initial time τ_c^{SB} . The initial cluster delay $\tau_c^{\text{SB}}(t_0)$ is generated by random variables $\Delta\tau_{c,\text{SB}}$ [31], where $\Delta\tau_{c,\text{SB}}$ is defined as the time interval of arrival between two adjacent clusters for the first order cluster and the second order cluster, respectively. For the first cluster, $\Delta\tau_{1,\text{SB}}$ is the time interval compared to the LoS path. So, we have

$$\tau_c^{\text{SB}}(t_0) = \begin{cases} D/c_0 + \Delta\tau_{c,\text{SB}}, & c = 1; \\ \tau_{c-1} + \Delta\tau_{c,\text{SB}}, & 2 \leq c \leq C_{\text{SB}}. \end{cases} \quad (11)$$

A similar method is used to generate MBCs expressed as

$$\tau_k^{\text{MB}}(t_0) = \begin{cases} D/c_0 + \Delta\tau_{k,\text{MB}}, & k = 1; \\ \tau_{k-1} + \Delta\tau_{k,\text{MB}}, & 2 \leq k \leq C_{\text{MB}}. \end{cases} \quad (12)$$

Here, $\Delta\tau_{c,\text{SB}}$ and $\Delta\tau_{k,\text{MB}}$ are exponential random variables with the mean values $\mu_{\Delta\tau_{\text{SB}}}$ and $\mu_{\Delta\tau_{\text{MB}}}$, respectively.

Considering the long traveling paths, after we generate the initial delay for SBC at t , the total delay of the cluster at $t + \Delta t$ can be calculated according to the geometric relationship in Fig. 2. When the Tx is fixed and the Rx moves, we extend the reflection surface closest to the Tx and obtain the mirror point of the Tx. When the Rx moves in a short period, the mirror point keeps static and the cluster slides for a short length at the surface. The solid line is the initial path and the dashed line represents the path after the Rx moves. Similarly, when the Rx is fixed and the Tx moves, we can also find the mirror point of the Rx for calculation. This method jointly considers the movement of the clusters and the Tx/Rx.

We denote A_p^T to represent the mirror point of A_p^T . It is clear that the distance from A_p^T to A_q^R at time t equals $D_{p,q,c}^{\text{SB}}(t)$. The vector $\vec{D}_{p,q,c}^{\text{SB}}(t)$ from A_p^T to A_q^R is

$$\vec{D}_{p,q,c}^{\text{SB}}(t) = D_{p,q,c}^{\text{SB}}(t) \cdot \begin{bmatrix} \cos \theta_{q,c}^{\text{SR}} \cos \phi_{q,c}^{\text{SR}} \\ \cos \theta_{q,c}^{\text{SR}} \sin \phi_{q,c}^{\text{SR}} \\ \sin \theta_{q,c}^{\text{SR}} \end{bmatrix}. \quad (13)$$

The vector $\vec{D}_{p,q,c}^{\text{SB}}(t + \Delta t)$ at time $t + \Delta t$ is easily calculated as

$$\begin{aligned} \vec{D}_{p,q,c}^{\text{SB}}(t + \Delta t) &= \vec{D}_{p,q,c}^{\text{SB}}(t) + \vec{v}^{\text{R}} \Delta t \\ &= D_{p,q,c}^{\text{SB}}(t) \begin{bmatrix} \cos \theta_{q,c}^{\text{SR}} \cos \phi_{q,c}^{\text{SR}} \\ \cos \theta_{q,c}^{\text{SR}} \sin \phi_{q,c}^{\text{SR}} \\ \sin \theta_{q,c}^{\text{SR}} \end{bmatrix} \\ &\quad + v_{\text{R}} \Delta t \cdot \begin{bmatrix} \cos \zeta^{\text{R}} \cos \xi^{\text{R}} \\ \cos \zeta^{\text{R}} \sin \xi^{\text{R}} \\ \sin \zeta^{\text{R}} \end{bmatrix}. \end{aligned} \quad (14)$$

The new distance from A_p^{T} to A_q^{R} at time $(t + \Delta t)$ denoted by $D_{p,q,c}^{\text{SB}}(t + \Delta t)$ can be calculated by

$$D_{p,q,c}^{\text{SB}}(t + \Delta t) = \left\| \vec{D}_{p,q,c}^{\text{SB}}(t + \Delta t) \right\|. \quad (15)$$

For the MBCs, when the Rx is moving, the mirror point of the Tx can be obtained by extending the line between Rx and last reflection point with the total path length. The virtual link is contained in the extended line so that this method can also be adopted in the MBCs. Considering the spatial non-stationarity of ultra-massive MIMO, the distance from A_p^{T} to A_q^{R} can be analogously obtained by using $\vec{\delta}_q$ to replace $\vec{v}^{\text{R}} \Delta t$ and can be calculated by

$$D_{p,q,c}^{\text{SB}}(t) = \left\| \vec{D}_c^{\text{SB}}(t) + \vec{\delta}_p \right\| \quad (16)$$

where

$$\vec{D}_c^{\text{SB}}(t) = D_c^{\text{SB}}(t) \begin{bmatrix} \cos \theta_c^{\text{SR}} \cos \phi_c^{\text{SR}} \\ \cos \theta_c^{\text{SR}} \sin \phi_c^{\text{SR}} \\ \sin \theta_c^{\text{SR}} \end{bmatrix}. \quad (17)$$

Here $D_c^{\text{SB}}(t)$ represents the total distance from the center of Tx to Rx via C_c^{S} .

The power of the cluster P_c^{SB} and P_k^{MB} is generated according to the delay of the paths [31]. We use SBC as an example and they can be expressed as

$$P_c^{\text{SB}}(\text{dB}) = -n_\tau \cdot (\tau_c^{\text{SB}} - \tau^{\text{LoS}}) + \Delta a_i \quad (18)$$

where n_τ is the temporal decay coefficient. Moreover, Δa_i is a Gaussian distributed random variable describing the random deviation of different clusters. After we generate the power of all clusters, we need to normalize these by the total power.

B. Frequency-Dependent Parameters

In THz bands, wavelength is comparable to the roughness of the reflection surface. In addition, scattering rays are closely related to the frequency, which is quite different from lower frequencies. The distribution of reflected power from one incident wave can be measured by scattering coefficient which was investigated in [27]. For an incident wave, the path with the strongest reflection is the specular reflection. However, the scattering around the specular reflection path also need to be considered. In [27], the average scattering coefficient $\langle \rho \rho^* \rangle_\infty$ is

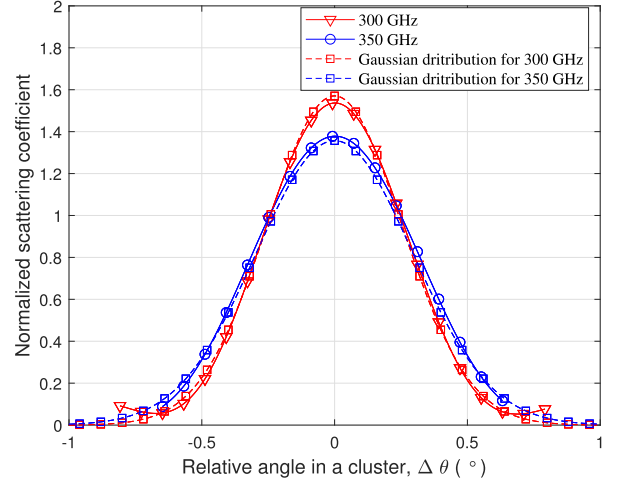


Fig. 3. The comparison of normalized scattering coefficients at different frequencies and fitting with Gaussian distribution ($\sigma = 0.25$ at 300 GHz, $\sigma = 0.29$ at 350 GHz, $l_{\text{corr}} = 2.3$ mm, $l_x = l_y = 10l_{\text{corr}}$, $\sigma_h = 0.13$ mm).

given, and can be calculated as

$$\langle \rho \rho^* \rangle_\infty = e^{-g} \cdot \left(\rho_0^2 + \frac{\pi l_{\text{corr}}^2 F^2}{A} \sum_{m=1}^{\infty} \frac{g^m}{m! m} e^{-\frac{v_{xy}^2 l_{\text{corr}}^2}{4m}} \right) \quad (19)$$

with

$$\rho_0 = \text{sinc}(v_x l_x) \cdot \text{sinc}(v_y l_y) \quad (20)$$

$$v_x = k \cdot (\sin(\theta_1) - \sin(\theta_2) \cos(\theta_3)) \quad (21)$$

$$v_y = k \cdot (-\sin(\theta_2) \sin(\theta_3)) \quad (22)$$

$$v_{xy} = \sqrt{v_x^2 + v_y^2} \quad (23)$$

$$F = \frac{1 + \cos(\theta_1) \cos(\theta_2) - \sin(\theta_1) \sin(\theta_2) \cos(\theta_3)}{\cos(\theta_1) (\cos(\theta_1) + \cos(\theta_2))} \quad (24)$$

$$g = k^2 \sigma_h^2 (\cos(\theta_1) + \cos(\theta_2))^2. \quad (25)$$

Here, $l_x \cdot l_y$ calculates the the rectangular surface area. The parameters σ_h and l_{corr} represent the standard deviation of heights and the surface correlation length, respectively, given in [27]. θ_1 , θ_2 , and θ_3 represent the incident angle, exit angle, and the angle between incident plane and exit plane, respectively. Parameter k is the wave number decided by frequency. According to these equations, the normalized scattering coefficients at different frequencies are compared in Fig. 3. It should be noticed that only the main lobe of the scattering beam is taken into consideration. From Fig. 3, we find that Gaussian distribution fits well with the main lobe at different frequencies. The standard deviation σ of scattered wave at 300 GHz is 0.25 and is 0.29 at 350 GHz. This means that the relative angle in each cluster can be considered as zero mean Gaussian distributed random variables.

Here, $\phi_{p,c,l}^{\text{ST}}$ is shown as an example. The azimuth angle of the l th ray in the c th cluster is

$$\phi_{p,c,l}^{\text{ST}} = \phi_{p,c}^{\text{ST}} + \Delta \phi_{p,c,l}^{\text{ST}} \quad (26)$$

where $\Delta\phi_{p,c,l}^{\text{ST}}$ is the relative angle for the l th ray in the c th cluster with respect to $\phi_{p,c}^{\text{ST}}$ and follows a Gaussian distribution with standard deviation of $\sigma_{c,\phi}^{\text{ST}}(f_i)$. The standard deviation $\sigma_{c,\phi}^{\text{ST}}(f_i)$ is considered as an exponential distributed random variable according to [32]

$$f_\mu(x) = \frac{1}{\mu} e^{-\frac{x}{\mu}} \quad (27)$$

where μ is the mean value of azimuth for the c th cluster described by parameter $\mu_{c,\phi}^{\text{ST}}$. Relative angles need to be regenerated at new frequencies and can be modeled as

$$\sigma_{c,\phi}^{\text{ST}}(f_i) = \sigma_{c,\phi}^{\text{ST}}(f_0) \times (f_i/f_0)^{\rho_\phi^{\text{ST}}} \quad (28)$$

where ρ_ϕ^{ST} represents the frequency-dependent factor for relative angle. The relative elevation and azimuth angles of clusters are considered as independent.

According to the relative angle, the total time of arrival of different scattering paths can be calculated by the geometric relationship as

$$D_{p,q,c,l}^{\text{SB}} = \sqrt{D_{p,q,c,l}^{\text{SB,V}^2} + D_{p,q,c,l}^{\text{SB,H}^2}} \quad (29)$$

where $D_{p,q,c,l}^{\text{SB,V}}$ and $D_{p,q,c,l}^{\text{SB,H}}$ represent the vertical and horizontal distances of the path length, respectively. They can be calculated by

$$D_{p,q,c,l}^{\text{SB,V}} = D_{p,q,c}^{\text{SB}} \sin(\theta_{q,c}^{\text{SR}}) r_c^{\text{SR}} / \cos(\Delta\theta_{p,c,l}^{\text{SR}}) + D_{p,q,c}^{\text{SB}} \sin(\theta_{q,c}^{\text{ST}}) r_c^{\text{ST}} / \cos(\Delta\theta_{p,c,l}^{\text{ST}}) \quad (30)$$

$$D_{p,q,c,l}^{\text{SB,H}} = D_{p,q,c}^{\text{SB}} \cos(\theta_{q,c}^{\text{SR}}) r_c^{\text{SR}} / \cos(\Delta\phi_{p,c,l}^{\text{SR}}) + D_{p,q,c}^{\text{SB}} \cos(\theta_{q,c}^{\text{ST}}) r_c^{\text{ST}} / \cos(\Delta\phi_{p,c,l}^{\text{ST}}) \quad (31)$$

where $r_c^{\text{ST(R)}}$ is the ratio of the distance between the cluster and the Tx(Rx) to the total distance. For SBCs, it is clear that $r_c^{\text{ST}} + r_c^{\text{SR}} = 1$. For MBCs, $r_c^{\text{ST}} + r_c^{\text{SR}} < 1$. When relative angles are updated in the frequency domain, corresponding total distances are also updated according to the geometric relationship in (29)–(31).

C. Channel Transfer Function

In this model, we divide the whole band into many small sub-bands with different CIR. As a result, we need to calculate the CTF of each sub-band and then combine them together. Fig. 4 is an example of adding up two sub-band channels. Similarly, we can add up more sub-band channels in the same manner.

The CTF of sub-band channel $H_{p,q}(t, f, f_i)$ is calculated as the Fourier transformation of the sub-band CIR, i.e.,

$$H_{p,q}(t, f, f_i) = \int_{-\infty}^{\infty} h_{p,q}(t, \tau, f_i) e^{-j2\pi f\tau} d\tau, f \in f_i. \quad (32)$$

The CTF of the whole band is given by

$$H_{p,q}(t, f) = \sum_{i=1}^{N_F} H_{p,q}(t, f, f_i). \quad (33)$$

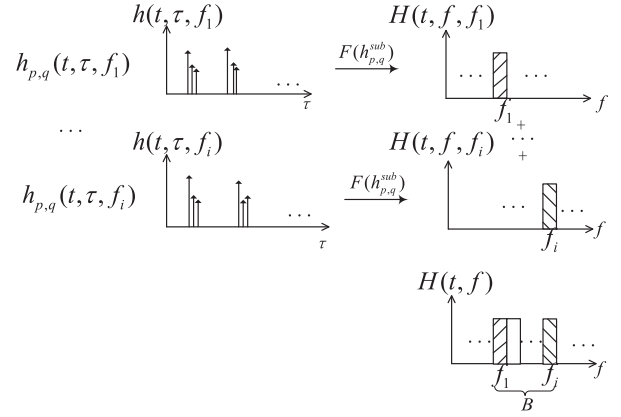


Fig. 4. An example of adding up two sub-band channels.

III. STATISTICAL PROPERTIES OF THE THEORETICAL MODEL

A. STFCF

The correlation between two arbitrary CIRs, $h_{p,q}(t, \tau, f_i)$ and $h_{p,q'}(t + \Delta t, \tau, f_i + \Delta f)$ at different times, spaces, and frequencies can be calculated by superimposing the correlation of all the clusters with the assumption of uncorrelated scattering. The correlation function of two arbitrary channels can be calculated as follows

$$R_h(p, q, p', q', t, \Delta t, f_i, \Delta f) = E [h_{p,q}(t, \tau, f_i) h_{p',q'}^*(t + \Delta t, \tau, f_i + \Delta f)] \quad (34)$$

where $(\cdot)^*$ is the complex conjugate operation, and $E[\cdot]$ calculates the expectation value by taking all 3D directions at both Tx and Rx sides into consideration. With the assumption of uncorrelated scatterers, the STFCF can be also written as

$$R_h(p, q, p', q', t, \Delta t, f_i, \Delta f) = R_h^{\text{LoS}}(p, q, p', q', t, \Delta t, f_i, \Delta f) + \sum_{c=1}^{C_{\text{SB}}} R_{h,c}^{\text{SB}}(p, q, p', q', t, \Delta t, f_i, \Delta f) + \sum_{k=1}^{C_{\text{MB}}} R_{h,k}^{\text{MB}}(p, q, p', q', t, \Delta t, f_i, \Delta f). \quad (35)$$

– In the LoS case,

$$R_h^{\text{LoS}}(p, q, p', q', t, \Delta t, f_i, \Delta f) = \frac{K}{K+1} e^{j2\pi(f_i\tau_{p,q}(t) - (f_i + \Delta f)\tau_{p',q'}(t + \Delta t))}. \quad (36)$$

– In the SB case,

$$R_{h,c}^{\text{SB}}(p, q, p', q', t, \Delta t, f_i, \Delta f) = \frac{P_c^{\text{SB}}}{K+1} \int_{-\pi}^{\pi} \int_{-\pi/2}^{\pi/2} \int_{-\pi}^{\pi} \int_{-\pi/2}^{\pi/2} e^{j2\pi(f_i\tau_{p,q}(t) - (f_i + \Delta f)\tau_{p',q'}(t + \Delta t))} f(\theta_{p,c}^{\text{ST}}) f(\phi_{p,c}^{\text{ST}}) f(\theta_{q,c}^{\text{SR}}) f(\phi_{q,c}^{\text{SR}}) d\theta_{p,c}^{\text{ST}} d\phi_{p,c}^{\text{ST}} d\theta_{q,c}^{\text{SR}} d\phi_{q,c}^{\text{SR}}. \quad (37)$$

– In the MB case,

$$R_{h,k}^{\text{MB}}(p, q, p', q', t, \Delta t, f_i, \Delta f) = \frac{P_k^{\text{MB}}}{K+1} \int_{-\pi}^{\pi} \int_{-\pi/2}^{\pi/2} \int_{-\pi}^{\pi} \int_{-\pi/2}^{\pi/2} e^{j2\pi(f_i\tau_{p,q}(t) - (f_i + \Delta f)\tau_{p',q'}(t + \Delta t))} f(\theta_{p,k}^{\text{MT}}) f(\phi_{p,k}^{\text{MT}}) f(\theta_{q,k}^{\text{MR}}) f(\phi_{q,k}^{\text{MR}}) d\theta_{p,k}^{\text{MT}} d\phi_{p,k}^{\text{MT}} d\theta_{q,k}^{\text{MR}} d\phi_{q,k}^{\text{MR}}. \quad (38)$$

B. Time Variant ACF

The time-variant ACF reflects the correlation between two channels at different instants. It can be calculated by setting $p' = p$, $q' = q$ and $\Delta f = 0$ in (34) and can be expressed as

$$r_h(p, q, t, \Delta t, f_i) = R_h(p, q, t, \Delta t, f_i) = r_h^{\text{LoS}}(p, q, t, \Delta t, f_i) + \sum_{c=1}^{C_{\text{SB}}} r_{h,c}^{\text{SB}}(p, q, t, \Delta t, f_i) + \sum_{k=1}^{C_{\text{MB}}} r_{h,k}^{\text{MB}}(p, q, t, \Delta t, f_i). \quad (39)$$

– In the LoS case,

$$r_h^{\text{LoS}}(p, q, t, \Delta t, f_i) = \frac{K}{K+1} e^{j2\pi f_i(\tau_{p,q}(t) - \tau_{p,q}(t + \Delta t))}. \quad (40)$$

– In the SB case,

$$r_{h,c}^{\text{SB}}(p, q, t, \Delta t, f_i) = \frac{P_c^{\text{SB}}}{K+1} \int_{-\pi}^{\pi} \int_{-\pi/2}^{\pi/2} \int_{-\pi}^{\pi} \int_{-\pi/2}^{\pi/2} e^{j2\pi f_i(\tau_{p,q}(t) - \tau_{p,q}(t + \Delta t))} f(\theta_{p,c}^{\text{ST}}) f(\phi_{p,c}^{\text{ST}}) f(\theta_{q,c}^{\text{SR}}) f(\phi_{q,c}^{\text{SR}}) d\theta_{p,c}^{\text{ST}} d\phi_{p,c}^{\text{ST}} d\theta_{q,c}^{\text{SR}} d\phi_{q,c}^{\text{SR}}. \quad (41)$$

– In the MB case,

$$r_{h,k}^{\text{MB}}(p, q, t, \Delta t, f_i) = \frac{P_k^{\text{MB}}}{K+1} \int_{-\pi}^{\pi} \int_{-\pi/2}^{\pi/2} \int_{-\pi}^{\pi} \int_{-\pi/2}^{\pi/2} e^{j2\pi f_i(\tau_{p,q}(t) - \tau_{p,q}(t + \Delta t))} f(\theta_{p,k}^{\text{MT}}) f(\phi_{p,k}^{\text{MT}}) f(\theta_{q,k}^{\text{MR}}) f(\phi_{q,k}^{\text{MR}}) d\theta_{p,k}^{\text{MT}} d\phi_{p,k}^{\text{MT}} d\theta_{q,k}^{\text{MR}} d\phi_{q,k}^{\text{MR}}. \quad (42)$$

C. Spatial CCF

From (34), the spatial CCF can be derived by imposing $\Delta t = 0$ and $\Delta f = 0$ and can be written as

$$\begin{aligned} \rho_h(p, q, p', q', t, f_i) &= R_h(p, q, p', q', t, f_i) \\ &= \rho_h^{\text{LoS}}(p, q, p', q', t, f_i) \\ &\quad + \sum_{c=1}^{C_{\text{SB}}} \rho_{h,c}^{\text{SB}}(p, q, p', q', t, f_i) \\ &\quad + \sum_{k=1}^{C_{\text{MB}}} \rho_{h,k}^{\text{MB}}(p, q, p', q', t, f_i). \end{aligned} \quad (43)$$

– In the LoS case,

$$\rho_h^{\text{LoS}}(p, q, p', q', t, f_i) = \frac{K}{K+1} e^{j2\pi f_i(\tau_{p,q}(t) - \tau_{p',q'}(t))}. \quad (44)$$

– In the SB case,

$$\rho_{h,c}^{\text{SB}}(p, q, p', q', t, f_i) = \frac{P_c^{\text{SB}}}{K+1} \int_{-\pi}^{\pi} \int_{-\pi/2}^{\pi/2} \int_{-\pi}^{\pi} \int_{-\pi/2}^{\pi/2} e^{j2\pi f_i(\tau_{p,q}(t) - \tau_{p',q'}(t))} f(\theta_{p,c}^{\text{ST}}) f(\phi_{p,c}^{\text{ST}}) f(\theta_{q,c}^{\text{SR}}) f(\phi_{q,c}^{\text{SR}}) d\theta_{p,c}^{\text{ST}} d\phi_{p,c}^{\text{ST}} d\theta_{q,c}^{\text{SR}} d\phi_{q,c}^{\text{SR}}. \quad (45)$$

– In the MB case,

$$\rho_{h,k}^{\text{MB}}(p, q, p', q', t, f_i) = \frac{P_k^{\text{MB}}}{K+1} \int_{-\pi}^{\pi} \int_{-\pi/2}^{\pi/2} \int_{-\pi}^{\pi} \int_{-\pi/2}^{\pi/2} e^{j2\pi f_i(\tau_{p,q}(t) - \tau_{p',q'}(t))} f(\theta_{p,k}^{\text{MT}}) f(\phi_{p,k}^{\text{MT}}) f(\theta_{q,k}^{\text{MR}}) f(\phi_{q,k}^{\text{MR}}) d\theta_{p,k}^{\text{MT}} d\phi_{p,k}^{\text{MT}} d\theta_{q,k}^{\text{MR}} d\phi_{q,k}^{\text{MR}}. \quad (46)$$

D. FCF

The FCF is another important channel statistical property reflecting the correlation of the channels at different frequencies. It can be calculated by

$$\begin{aligned} T_h(p, q, t, f, \Delta f) &= E [H_{p,q}(t, f) \cdot H_{p,q}^*(t, f + \Delta f)] \\ &= E \left[\int_{-\infty}^{\infty} h_{p,q}(t, \tau, f) e^{-j2\pi f \tau} d\tau \int_{-\infty}^{\infty} h_{p,q}(t, \tau, f + \Delta f) e^{-j2\pi f \tau} d\tau \right]. \end{aligned} \quad (47)$$

IV. THE SIMULATION MODEL AND STATISTICAL PROPERTIES

A. Description of the Simulation Model

In the aforementioned theoretical channel model, each cluster is composed of an infinite number of rays, which can not be implemented in hardware or software. According to the theoretical model, the simulation model comprises finite rays in each cluster expressed as

$$\begin{aligned} \tilde{h}_{p,q}(t, \tau, f_i) &= \tilde{h}_{p,q}^{\text{LoS}}(t, \tau, f_i) + \sum_{c=1}^{C_{\text{SB}}} \tilde{h}_{p,q,c}^{\text{SB}}(t, \tau, f_i) \\ &\quad + \sum_{k=1}^{C_{\text{MB}}} \tilde{h}_{p,q,k}^{\text{MB}}(t, \tau, f_i) \end{aligned} \quad (48)$$

where the LoS part is expressed as

$$\tilde{h}_{p,q}^{\text{LoS}}(t, \tau, f_i) = \sqrt{\frac{K}{K+1}} \times e^{-j(2\pi f_i \tau_{p,q}^{\text{LoS}}(t))} \delta(\tau - \tau_{p,q}^{\text{LoS}}(t)). \quad (49)$$

The SB and MB components of the simulation model are

$$\tilde{h}_{p,q,c}^{\text{SB}}(t, \tau, f_i) = \sqrt{\frac{P_c^{\text{SB}}}{K+1}} \sum_{l=1}^{L_c} \sqrt{\frac{1}{L_c}} e^{-j(2\pi f_i \tau_{p,q,c,l}^{\text{SB}}(t) - \Theta_{c,l}^{\text{SB}})} \delta(\tau - \tau_{p,q,c,l}^{\text{SB}}(t)) \quad (50)$$

$$\tilde{h}_{p,q,k}^{\text{MB}}(t, \tau, f_i) = \sqrt{\frac{P_k^{\text{MB}}}{K+1}} \sum_{m=1}^{M_k} \sqrt{\frac{1}{M_k}} e^{-j(2\pi f_i \tau_{p,q,c,m}^{\text{MB}}(t) - \Theta_{c,m}^{\text{MB}})} \delta(\tau - \tau_{p,q,c,m}^{\text{MB}}(t)). \quad (51)$$

In this simulation model, relative angles are discrete for simulation. In each cluster, maximum relative angle corresponds to maximum relative delay so that the discrete relative delay can be generated by relative angles. Hence, an appropriate parameter calculation method is necessary to approximate the properties of the theoretical channel model. In this simulation model, we apply the MEA [47] method to generate the discrete angles. In this simulation model, the MEA method is used to calculate limited discrete angles according to principle that the integral of the probability between two adjacent angles are equal.

Here, we use $\theta_{p,c,l}^{\text{ST}}$ as an example to generate $\sqrt{L_c}$ discrete values with the MEA method. The whole probability are divided into $\sqrt{L_c}$ parts with the same area $1/\sqrt{L_c}$. According to the equation $\int_{l-1}^l dF(x) = 1/\sqrt{L_c}$ where $F(x)$ is the cumulative distribution function (CDF) of $\theta_{p,c,l}^{\text{ST}}$, then $\sqrt{L_c}$ discrete angle can be obtained. Similarly, the $\phi_{p,c,l}^{\text{ST}}$ can also generate $\sqrt{L_c}$ discrete values. So there are L_c discrete values in this cluster. Meanwhile, the discrete $\theta_{q,c,l}^{\text{SR}}$ and $\phi_{q,c,l}^{\text{SR}}$ can also be obtained.

B. Statistical Properties of the Simulation Model

In this sub-section, the statistical properties of the non-stationary THz simulated model are derived.

1) *STFCF*: The STFCF of the simulation model $\tilde{R}_h(p, q, p', q', t, \Delta t, f, \Delta f)$ can be represented as

$$\begin{aligned} & \tilde{R}_h(p, q, p', q', t, \Delta t, f, \Delta f) \\ &= E \left[\tilde{h}_{p,q}(t, f_i) \cdot \tilde{h}_{p',q'}^*(t + \Delta t, f + \Delta f) \right] \\ &= \tilde{R}_h^{\text{LoS}}(p, q, p', q', t, \Delta t, f_i, \Delta f) \\ &+ \sum_{c=1}^{C_{\text{SB}}} \tilde{R}_{n,c}^{\text{SB}}(p, q, p', q', t, \Delta t, f_i, \Delta f) \\ &+ \sum_{k=1}^{C_{\text{MB}}} \tilde{R}_{h,k}^{\text{MB}}(p, q, p', q', t, \Delta t, f_i, \Delta f). \quad (52) \end{aligned}$$

The correlation function of the channel also consists of the LoS, SBCs, and MBCs. –In the LoS case,

$$\tilde{R}_h^{\text{LoS}}(p, q, p', q', t, \Delta t, f_i, \Delta f) = \frac{K}{K+1} e^{j2\pi(f_i \tau_{p,q}(t) - (f_i + \Delta f) \tau_{p',q'}(t + \Delta t))}. \quad (53)$$

–In the SB case,

$$\tilde{R}_{h,c}^{\text{SB}}(p, q, p', q', t, \Delta t, f_i, \Delta f) = \frac{P_c^{\text{SB}}}{K+1} \sum_{l=1}^{L_c} e^{j2\pi(f_i \tau_{p,q}(t) - (f_i + \Delta f) \tau_{p',q'}(t + \Delta t))}. \quad (54)$$

–In the MB case,

$$\tilde{R}_{h,k}^{\text{MB}}(p, q, p', q', t, \Delta t, f_i, \Delta f) = \frac{P_k^{\text{MB}}}{K+1} \sum_{m=1}^{M_k} e^{j2\pi(f_i \tau_{p,q}(t) - (f_i + \Delta f) \tau_{p',q'}(t + \Delta t))}. \quad (55)$$

By setting partial parameters of $(\Delta p, \Delta q, \Delta t, \Delta f)$ as 0, the STFCF can easily be simplified to time-variant ACF, spatial CCF, and FCF.

2) *The Delay PSD*: The delay PSD of the simulation model $\Upsilon_{p,q}(t, \tau, f_i)$ is calculated as

$$\begin{aligned} \Upsilon_{p,q}(t, \tau, f_i) &= \left| \tilde{h}_{p,q}(t, \tau, f_i) \right|^2 \\ &= \left| \tilde{h}_{p,q}^{\text{LoS}}(t, \tau, f_i) \right|^2 + \sum_{c=1}^{C_{\text{SB}}} \left| \tilde{h}_{p,q,c}^{\text{SB}}(t, \tau, f_i) \right|^2 \\ &+ \sum_{k=1}^{C_{\text{MB}}} \left| \tilde{h}_{p,q,k}^{\text{MB}}(t, \tau, f_i) \right|^2. \quad (56) \end{aligned}$$

It should be noted that the time-space-frequency variant properties of delay PSD is caused by the time-space-frequency variant powers and delays.

3) *The Stationary Intervals*: The stationary interval is the time, distance, and frequency bandwidth during which the propagation channel can be considered as unchanged in time, space, and frequency domains, respectively. The stationary interval is defined as the maximum length within which the ACF of the time-space-frequency variant delay PSD exceeds the threshold [48]. Here we calculate the stationary interval in time and frequency domains expressed as $I(\Delta t, \Delta f) = \inf\{\Delta t, \Delta f \mid R_{\Upsilon}(t, f, \Delta t, \Delta f) < c_{th}\}$ where $\inf\{\cdot\}$ calculates the infimum of a function. The normalized ACF of the delay PSD $R_{\Lambda}(t, f, \Delta t, \Delta f)$ is defined by

$$\begin{aligned} R_{\Lambda}(t, f_i, \Delta t, \Delta f) &= \\ & \frac{\int \Upsilon_{p,q}(t, \tau, f_i) \Upsilon_{p,q}(t_i + \Delta t, \tau, f_i + \Delta f) d\tau}{\max \left\{ \int \Upsilon_{p,q}^2(t, \tau, f_i) d\tau, \int \Upsilon_{p,q}^2(t_i + \Delta t, \tau, f_i + \Delta f) d\tau \right\}}. \quad (57) \end{aligned}$$

V. RESULTS AND ANALYSIS

In this section, the statistical properties of the THz channel models are simulated and discussed. The frequency band is chosen from 300 GHz to 350 GHz. The numbers of antenna elements at the Tx and Rx are 256 at both Tx and Rx. Both δ_T and δ_R equal to half of wavelength at 325 GHz. The moving speed of Rx is $v^R = 0.1$ m/s with the direction angle $\zeta^R = 0$ and $\xi^R = \frac{\pi}{3}$ while the Tx is fixed. The bandwidth of sub-band is

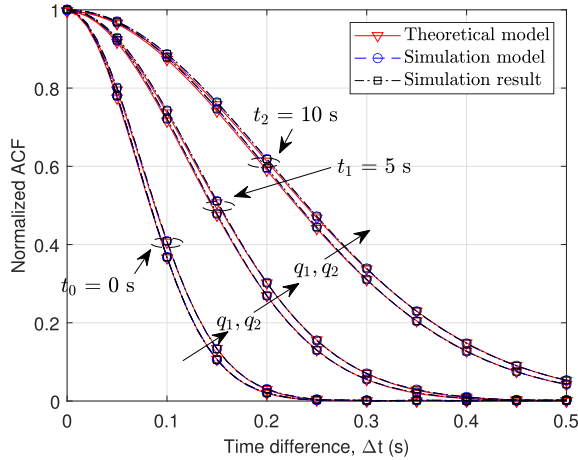


Fig. 5. The comparison of time-variant ACFs of theoretical model, simulation model, and simulation results for cluster C_1^S at $t_0 = 0$ s, $t_1 = 5$ s and $t_2 = 10$ s with $q_1 = 1$ and $q_2 = 200$ ($D = 3$ m, $p = 1$, $f_0 = 325$ GHz, $v^R = 0.1$ m/s, $\zeta^R = 0$, $\xi^R = \frac{\pi}{3}$, $\mu_{c,\theta}^{SR} = 1.4^\circ$, $\mu_{c,\phi}^{SR} = 2.8^\circ$, $r_c^{ST} = 0.4$).

0.1 GHz. It should be noted that it is less than the real stationary bandwidth to make sure that each sub-band in the simulation is frequency stationary. The number of rays in each cluster is $L_c = M_c = 400$.

A. ACF

The time ACF of the model can be calculated by setting $\Delta p, \Delta q, \Delta f$ as 0. The comparison of theoretical model, simulation model, and simulation result at $t_0 = 0$ s, $t_1 = 5$ s, and $t_2 = 10$ s of Cluster₁ at different antennas is shown in Fig. 5. From the results, we can observe that the simulation models fit well with the theoretical model and the simulation results. We can also observe different time ACFs at different time instants, showing the non-stationarity in time domain. The difference between different receive antennas can also be observed clearly showing the non-stationarity of ultra-massive MIMO.

B. Spatial CCF

The spatial CCFs of the theoretical model, simulation model, and simulation result for Cluster₁ at different time and different frequencies are shown in Fig. 6. We can see that the theoretical model, simulation model, and simulation result match very well. We can also observe significant differences at different time instants. Due to the traveling of the Rx, the channel shows non-stationarity in the time domain. In addition, we present the results in different frequencies showing unnegligible frequency non-stationarity. For higher frequencies, the spatial CCFs tend to be smaller.

C. FCF

The absolute values of FCFs for NLoS paths at different $f_0 = 300$ GHz, $f_1 = 325$ GHz, and $f_2 = 350$ GHz for THz massive MIMO channel model are shown in Fig. 7. We can notice that differences among FCFs at different frequencies are

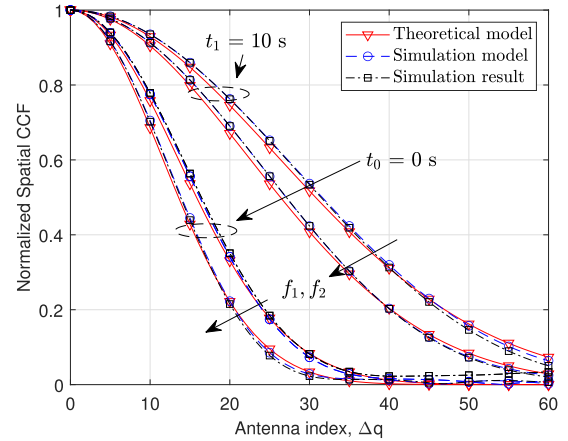


Fig. 6. The comparison of spatial CCFs of theoretical model, simulation model, and simulation results for cluster C_1^S ($D = 3$ m, $p = 1$, $q = 1$, $t_0 = 0$ s, $t_1 = 10$ s, $f_1 = 300$ GHz, $f_2 = 350$ GHz, $v^R = 0.1$ m/s, $\zeta^R = 0$, $\xi^R = \frac{\pi}{3}$, $\alpha^R = \frac{\pi}{3}$, $\beta^R = \frac{\pi}{4}$, $\mu_{c,\theta}^{SR} = 1.4^\circ$, $\mu_{c,\phi}^{SR} = 2.8^\circ$, $r_c^{ST} = 0.4$).

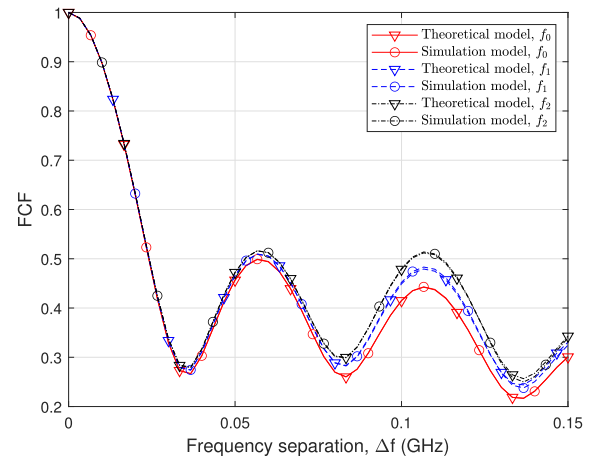


Fig. 7. The comparison of FCFs of theoretical model and simulation model at $f_0 = 300$ GHz, $f_1 = 325$ GHz and $f_2 = 350$ GHz ($D = 3$ m, $p = 1$, $q = 1$, $t_0 = 0$ s, $v^R = 0$ m/s, $\mu_{c,\theta}^{ST} = 1.2^\circ$, $\mu_{c,\phi}^{ST} = 1.7^\circ$, $\mu_{c,\theta}^{SR} = 1.4^\circ$, $\mu_{c,\phi}^{SR} = 2.8^\circ$, $\mu_c^{ToA} = 0.3$ ns, $\rho_\phi^{ST} = \rho_\phi^{ST} = \rho_\phi^{SR} = \rho_\phi^{SR} = 1.2$).

small but still observable which means that the non-stationarity in the frequency domain needs to be considered. When frequency difference increases, the gaps between different frequencies will also increase because the change rate of frequency correlation is related to the center frequency.

D. Stationary Bandwidth

The stationary bandwidth is simulated with parameters of a typical indoor scenario according to [31], [49]. The initial distance between the first elements of Tx and Rx is 3 m, $\mu_{\Delta\tau_{c,SB}}$ and $\mu_{\Delta\tau_{k,MB}}$ are set as 2.73 ns and 2.33 ns. The initial intra-cluster parameters $\mu_{c,\theta}^{ST}$, $\mu_{c,\phi}^{ST}$, $\mu_{c,\theta}^{SR}$, and $\mu_{c,\phi}^{SR}$ are set as 1.2° , 1.7° , 1.4° , and 2.8° , respectively. The mean value of relative time of arrival μ_c^{ToA} is set as 0.3 ns. The CDFs of the stationary bandwidth of the simulation channel model at different frequencies are shown

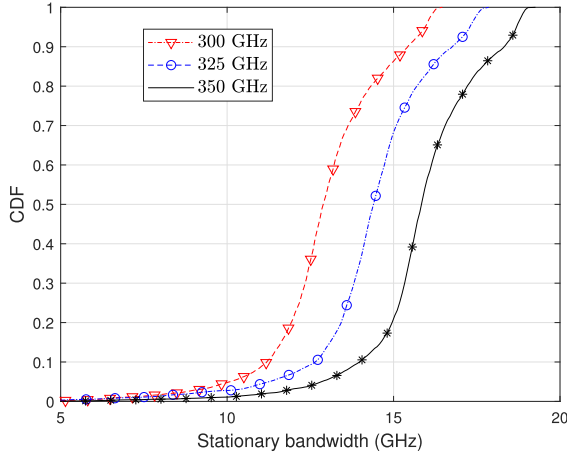


Fig. 8. The CDFs of stationary interval of the simulation model in frequency domain at $f_0 = 300$ GHz, $f_1 = 325$ GHz and $f_2 = 350$ GHz ($D = 3$ m, $p = 1$, $q = 1$, $t_0 = 0$ s, $v^R = 0.1$ m/s, $\mu_{c,\theta}^{ST} = 1.2^\circ$, $\mu_{c,\phi}^{ST} = 1.7^\circ$, $\mu_{c,\theta}^{SR} = 1.4^\circ$, $\mu_{c,\phi}^{SR} = 2.8^\circ$, $\mu_c^{ToA} = 0.3$ ns, $\rho_\phi^{ST} = \rho_\phi^{SR} = \rho_\phi^{SR} = \rho_\phi^{SR} = 1.2$, $c_{th} = 0.9$).

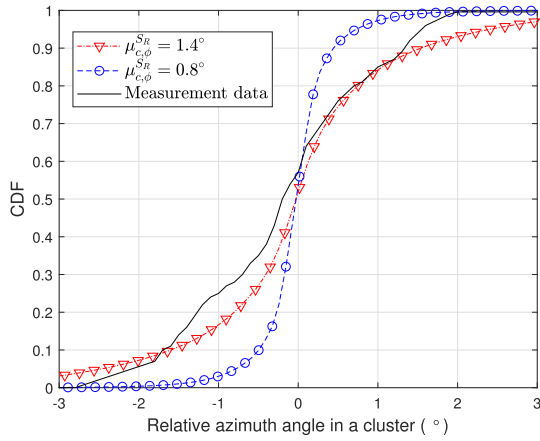


Fig. 9. The CDFs of relative angle in a cluster with different $\mu_{c,\phi}^{SR}$ and the measurement in [23] ($D = 2.7$ m, $p = 1$, $q = 1$, $t_0 = 0$ s, $f_0 = 300$ GHz, $v^R = 0$ m/s).

in Fig. 8. The threshold is chosen as 0.9. The median of the stationary bandwidth at 300 GHz is approximately 12.5 GHz. Higher frequency band has larger frequency stationary bandwidth. If the bandwidth in THz communication is large than the stationary bandwidth, non-stationarity in frequency domain is unneglectable.

E. Cluster Level Angle Spread

Cluster level angle spread reflect the degree of diffusely scattering in a cluster. In this simulation, the parameter $\mu_{c,\phi}^{SR}$ are estimated by using an optimization algorithm in order to fit the statistical properties of the channel model to those of the data from measurement [23] or ray tracing [32]. In the curve fitting (optimization) process, random initial values of those parameters were initialized. Then, the average mean square error of the simulation and measurement results is minimized by optimizing the values of those parameters in an iterative procedure. After

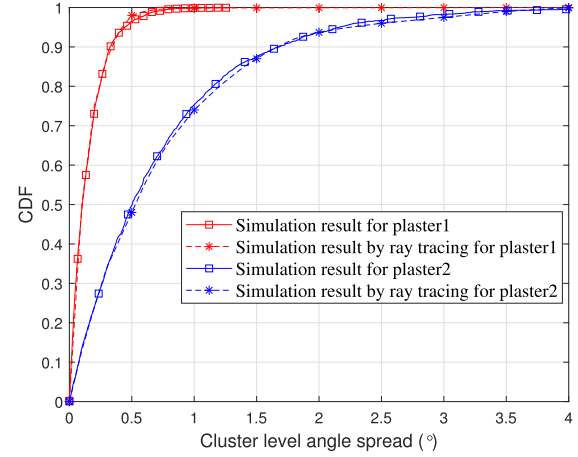


Fig. 10. The comparison of cluster level angular spread with different materials ($p = 1$, $q = 1$, $t_0 = 0$ s, $f_0 = 300$ GHz, $v^R = 0$ m/s, $r_c^{ST} = 0.4$, $\mu_{c,\phi}^{SR} = 0.15^\circ$ for plaster1, $\mu_{c,\phi}^{SR} = 0.75^\circ$ for plaster2).

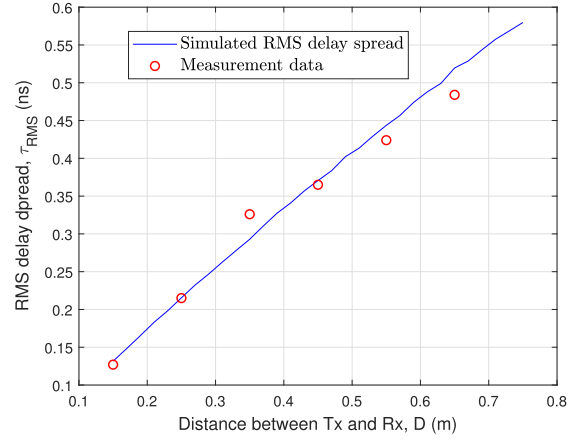


Fig. 11. The comparison of simulated RMS delay spread and measurement in [50] ($p = 1$, $q = 1$, $t_0 = 0$ s, $f_0 = 300$ GHz, $v^R = 0$ m/s, $\mu_{\Delta\tau_{SB}} = 0.08$, $\mu_{\Delta\tau_{MB}} = 0.07$ for $D = 0.15$ m).

the sufficient numbers of iterations, the optimal values of those parameters with the minimum mean square error can be found, which allows the desirable good fitting between the statistical property of the simulation model and measurement data. Firstly, the CDFs of relative azimuth angles of arrival with different $\mu_{c,\phi}^{SR}$ are simulated and compared with the measurement data [23] in Fig. 9. When the parameter $\mu_{c,\phi}^{SR}$ increases, the CDF of relative angles will be more gentle. We can observe the good agreement when $\mu_{c,\phi}^{SR} = 1.4^\circ$ indicating that the modeling methods can be applied to simulate realistic environments. Then we simulate the scattering in two materials with different roughness. The cluster level angle spread is greatly affected by the roughness of the material. The height standard deviation of plaster1 is $\sigma_{\text{plaster1}} = 0.5$ mm and $\sigma_{\text{plaster2}} = 1.5$ mm in [32]. Fig. 10 demonstrates the comparison of cluster level angle spread with different materials in this model and simulation by ray tracing in [32]. The results indicate that the proposed model can correctly approximate the results from ray tracing for different materials.

F. RMS Delay Spread

The RMS delay spread is simulated and fitted with the measurement data [50] by minimum mean square error criterion in Fig. 11 for short range communication where the transmission distance is less than 1 m. In the simulation, the parameters $\mu_{\Delta\tau_{c,SB}}$ and $\mu_{\Delta\tau_{k,MB}}$ are linearly increase with the LoS distance and the parameters at $D = 0.15$ m are estimated. We can observe good agreement between the simulation results and the measurement data. It means that the proposed model is suitable for this scenario.

VI. CONCLUSION

Novel 3D space-time-frequency non-stationary ultra-massive MIMO THz channel models have been proposed for 6G wireless communication systems with long traveling paths. Considering the unique propagation characteristics of THz bands, i.e., frequency-dependent diffusely scattering, relative angles and delays of rays within one cluster have been assumed to be frequency variant parameters. The statistical properties such as ACF, spatial CCF, and FCF have been derived for the proposed theoretical model and corresponding simulation model based on the MEA. Numerical results have shown that the statistical properties of the simulation model, verified by simulation results, can match well with those of the theoretical model. The good agreements between simulated results and corresponding measurements in different scenarios have further demonstrated the accuracy and good flexibility of the proposed model.

REFERENCES

- [1] M. Shafi *et al.*, "5G: A tutorial overview of standards, trials, challenges, deployment, and practice," *IEEE J. Sel. Areas Commun.*, vol. 35, no. 6, pp. 1201–1221, Jun. 2017.
- [2] X.-H. You *et al.*, "Towards 6G wireless communication networks: Vision, enabling technologies, and new paradigm shifts," *Sci. China Inf. Sci.*, vol. 64, no. 1, pp. 1–74, Jan. 2021.
- [3] C.-X. Wang, J. Huang, H. Wang, X. Gao, X.-H. You, and Y. Hao, "6G oriented wireless communication channel characteristics analysis and modeling," *Chin. J. Internet Things*, vol. 4, no. 1, pp. 19–32, Mar. 2020.
- [4] C.-X. Wang, J. Huang, H. Wang, X. Gao, X.-H. You, and Y. Hao, "6G wireless channel measurements and models: Trends and challenges," *IEEE Veh. Technol. Mag.*, vol. 15, no. 4, pp. 22–32, Dec. 2020.
- [5] S. Mumtaz, J. Jornet, J. Aulin, W. H. Gerstacker, X. Dong, and B. Ai, "Terahertz communication for vehicular networks," *IEEE Trans. Veh. Technol.*, vol. 66, no. 7, pp. 5617–5625, Jul. 2017.
- [6] Z. Chen *et al.*, "A survey on terahertz communications," *China Commun.*, vol. 16, no. 2, pp. 1–35, Feb. 2019.
- [7] B. Peng and T. Kürner, "A stochastic channel model for future wireless THz data centers," in *Proc. Int. Symp. Wireless Commun. Syst.*, Brussels, Belgium, Aug. 2015, pp. 741–745.
- [8] C. Cheng, S. Sangodoyin, and A. Zajić, "THz cluster-based modeling and propagation characterization in a data center environment," *IEEE Access*, vol. 8, pp. 56 544–56 558, 2020.
- [9] D. He *et al.*, "Channel modeling for kiosk downloading communication system at 300 GHz," in *Proc. 11th Eur. Conf. Antennas Propag.*, Paris, France, Mar. 2017, pp. 1331–1335.
- [10] D. He *et al.*, "Stochastic channel modeling for kiosk applications in the terahertz band," *IEEE Trans. THz Sci. Technol.*, vol. 7, no. 5, pp. 502–513, Sep. 2017.
- [11] K. Guan *et al.*, "On millimeter wave and THz mobile radio channel for smart rail mobility," *IEEE Trans. Veh. Technol.*, vol. 66, no. 7, pp. 5658–5674, Jul. 2017.
- [12] K. Guan *et al.*, "Measurement, simulation, and characterization of train-to-infrastructure inside-station channel at the terahertz band," *IEEE Trans. THz Sci. Technol.*, vol. 9, no. 3, pp. 291–306, May 2019.
- [13] K. Guan *et al.*, "Channel characterization for intra-wagon communication at 60 and 300 GHz bands," *IEEE Trans. Veh. Technol.*, vol. 68, no. 6, pp. 5193–5207, Jun. 2019.
- [14] S. Abadal, C. Han, and J. M. Jornet, "Wave propagation and channel modeling in chip-scale wireless communications: A survey from millimeter-wave to terahertz and optics," *IEEE Access*, vol. 8, pp. 278–293, 2020.
- [15] C. Han and I. F. Akyildiz, "Three-dimensional end-to-end modeling and analysis for graphene-enabled terahertz band communications," *IEEE Trans. Veh. Technol.*, vol. 66, no. 7, pp. 5626–5634, Jul. 2017.
- [16] S. Kim and A. Zajić, "Characterization of 300-GHz wireless channel on a computer motherboard," *IEEE Trans. Antennas Propag.*, vol. 64, no. 12, pp. 5411–5423, Dec. 2016.
- [17] K. Yang, A. Pellegrini, M. O. Munoz, A. Brizzi, A. Alomainy, and Y. Hao, "Numerical analysis and characterization of THz propagation channel for body-centric nano-communications," *IEEE Trans. THz Sci. Technol.*, vol. 5, no. 3, pp. 419–426, May 2015.
- [18] C. Belem-Goncalves *et al.*, "THz links using tube amplifiers and steerable beams for indoor applications," in *Proc. 44th Int. Conf. Infrared, Millimeter, Terahertz Waves*, Paris, France, Sep. 2019, pp. 1–2.
- [19] A. Brizzi, A. Pellegrini, L. Zhang, and Y. Hao, "Statistical path-Loss model for on-body communications at 94 GHz," *IEEE Trans. Antennas Propag.*, vol. 61, no. 11, pp. 5744–5753, Nov. 2013.
- [20] A. Pellegrini *et al.*, "Antennas and propagation for body-centric wireless communications at millimeter-wave frequencies: A review," *IEEE Antennas Propag. Mag.*, vol. 55, no. 4, pp. 262–287, Aug. 2013.
- [21] C. Jansen, R. Piesiewicz, D. Mittleman, T. Kürner, and M. Koch, "The impact of reflections from stratified building materials on the wave propagation in future indoor terahertz communication systems," *IEEE Trans. Antennas Propag.*, vol. 56, no. 5, pp. 1413–1419, May 2008.
- [22] R. Piesiewicz, C. Jansen, M. Koch, and T. Kürner, "Measurements and modeling of multiple reflections effect in building materials for indoor communication systems at THz frequencies," in *Proc. German Microw. Conf.*, Harburg, Germany, Mar. 2008, pp. 1–4.
- [23] S. Priebe, M. Kannicht, M. Jacob, and T. Kürner, "Ultra broadband indoor channel measurements and calibrated ray tracing propagation modeling at THz frequencies," *J. Commun. Netw.*, vol. 15, no. 6, pp. 547–558, Dec. 2013.
- [24] C. Jansen *et al.*, "Diffuse scattering from rough surfaces in THz communication channels," *IEEE Trans. THz Sci. Technol.*, vol. 1, no. 2, pp. 462–472, Nov. 2011.
- [25] F. Sheikh, D. Lessy, and T. Kaiser, "A novel ray-tracing algorithm for non-specular diffuse scattered rays at terahertz frequencies," in *Proc. 1st Int. Workshop Mobile THz Syst.*, Duisburg, Germany, Jul. 2018, pp. 1–6.
- [26] F. Sheikh and T. Kaiser, "Rough surface analysis for short-range ultra-broadband THz communications," in *Proc. IEEE Int. Symp. Antennas Propag. USNC/URSI Nat. Radio Sci. Meeting*, Boston, USA, Jul. 2018, pp. 1543–1544.
- [27] S. Priebe, M. Jacob, C. Jansen, and T. Kürner, "Non-specular scattering modeling for THz propagation simulations," in *Proc. 5th Eur. Conf. Antennas Propag.*, Rome, Italy, Apr. 2011, pp. 1–5.
- [28] S. Ju *et al.*, "Scattering mechanisms and modeling for terahertz wireless communications," in *Proc. ICC IEEE Int. Conf. Commun.*, Shanghai, China, May, 2019, pp. 1–7.
- [29] C. Han, A. O. Bicen, and I. F. Akyildiz, "Multi-ray channel modeling and wideband characterization for wireless communications in the terahertz band," *IEEE Trans. Wireless Commun.*, vol. 14, no. 5, pp. 2402–2412, May 2015.
- [30] S. Nie and I. F. Akyildiz, "Three-dimensional dynamic channel modeling and tracking for terahertz band indoor communications," in *Proc. IEEE 28th Annu. Int. Symp. Pers., Indoor, Mobile Radio Commun.*, Montreal, QC, Canada, Oct. 2017, pp. 1–5.
- [31] S. Priebe and T. Kürner, "Stochastic modeling of THz indoor radio channels," *IEEE Trans. Wireless Commun.*, vol. 12, no. 9, pp. 4445–4455, Sep. 2013.
- [32] S. Priebe, M. Jacob, and T. Kürner, "Angular and RMS delay spread modeling in view of THz indoor communication systems," *Radio Sci.*, vol. 49, no. 3, pp. 242–251, Mar. 2014.
- [33] N. A. Abbasi, A. Hariharan, A. M. Nair, and A. F. Molisch, "Channel measurements and path loss modeling for indoor THz communication," in *Proc. 14th Eur. Conf. Antennas Propag.*, Copenhagen, Denmark, 2020, pp. 1–5.
- [34] C.-X. Wang, J. Bian, J. Sun, W. Zhang, and M. Zhang, "A survey of 5G channel measurements and models," *IEEE Commun. Surv. Tut.*, vol. 20, no. 4, pp. 3142–3168, Oct.–Dec. 2018.

- [35] J. Bian, C.-X. Wang, X. Gao, X. You, and M. Zhang, "A general 3D non-stationary wireless channel model for 5G and beyond," *IEEE Trans. Wireless Commun.*, vol. 20, no. 5, pp. 3211–3224, May 2021.
- [36] S. Wu, C.-X. Wang, M. Aggoune, M. M. Alwakeel, and X. You, "A general 3D non-stationary 5G wireless channel model," *IEEE Trans. Commun.*, vol. 66, no. 7, pp. 3065–3078, Jul. 2018.
- [37] S. Wu, C.-X. Wang, H. Aggoune, M. M. Alwakeel, and Y. He, "A non-stationary 3D wideband twin-cluster model for 5G massive MIMO channels," *IEEE J. Sel. Areas Commun.*, vol. 32, no. 6, pp. 1207–1218, Jun. 2014.
- [38] S. Wu, C.-X. Wang, H. Haas, H. Aggoune, M. M. Alwakeel, and B. Ai, "A non-stationary wideband channel model for massive MIMO communication systems," *IEEE Trans. Wireless Commun.*, vol. 14, no. 3, pp. 1434–1446, Mar. 2015.
- [39] C. F. Lopez and C.-X. Wang, "Novel 3D non-stationary wideband models for massive MIMO channels," *IEEE Trans. Wireless Commun.*, vol. 17, no. 5, pp. 2893–2905, May 2018.
- [40] J. Huang, C.-X. Wang, R. Feng, J. Sun, W. Zhang, and Y. Yang, "Multi-frequency mmWave massive MIMO channel measurements and characterization for 5G wireless communication systems," *IEEE J. Sel. Areas Commun.*, vol. 35, no. 7, pp. 1591–1605, Jul. 2017.
- [41] J. Huang, C.-X. Wang, H. Chang, J. Sun, and X. Gao, "Multi-frequency multi-scenario millimeter wave MIMO channel measurements and modeling for B5G wireless communication systems," *IEEE J. Sel. Areas Commun.*, vol. 38, no. 9, pp. 2010–2025, Sep. 2020.
- [42] J. Huang, C.-X. Wang, Y. Liu, J. Sun, and W. Zhang, "A novel 3D GBMS for mmWave MIMO channels," *Sci. China Inf. Sci.*, vol. 61, no. 10, Oct. 2018, doi: [10.1007/s11432-018-9480-4](https://doi.org/10.1007/s11432-018-9480-4).
- [43] R. He, B. Ai, G. L. Stuber, G. Wang, and Z. Zhong, "Geometrical based modeling for millimeter wave MIMO mobile-to-mobile channels," *IEEE Trans. Veh. Technol.*, vol. 67, no. 4, pp. 2848–2863, Apr. 2018.
- [44] J. Wang, C.-X. Wang, J. Huang, and H. Wang, "A novel 3D space-time-frequency non-stationary channel model for 6G THz indoor communication systems," in *Proc. IEEE Wireless Commun. Netw. Conf.*, Apr. 2020, pp. 1–7.
- [45] J. Wang, C.-X. Wang, J. Huang, H. Wang, and X. Gao, "A general 3D space-time-frequency non-stationary THz channel model for 6G ultra massive MIMO wireless communication systems," *IEEE J. Sel. Areas Commun.*, vol. 39, no. 6, pp. 1576–1589, Jun. 2021.
- [46] A. A. M. Saleh and R. Valenzuela, "A statistical model for indoor multipath propagation," *IEEE J. Sel. Areas Commun.*, vol. 5, no. 2, pp. 128–137, Feb. 1987.
- [47] M. Pätzold, *Mobile Radio Channels, 2nd ed.* West, Sussex, U.K.: Wiley, 2012.
- [48] R. He *et al.*, "Characterization of quasi-stationarity regions for vehicle-to-vehicle radio channels," *IEEE Trans. Antennas Propag.*, vol. 63, no. 5, pp. 2237–2251, May 2015.
- [49] S. Priebe, M. Jacob, and T. Kürner, "AoA, AoD and ToA characteristics of scattered multipath clusters for THz indoor channel modeling," in *Proc. 17th Eur. Wireless 2011-Sustain. Wireless Technol.*, Apr. 2011, pp. 1–9.
- [50] S. Kim and A. G. Zajić, "Statistical characterization of 300 GHz propagation on a desktop," *IEEE Trans. Veh. Technol.*, vol. 64, no. 8, pp. 3330–3338, Aug. 2015.



Jun Wang (Student Member, IEEE) received the B.E. degree in 2016 in information engineering from Southeast University, Nanjing, China, where he is currently working toward the Ph.D. degree with National Mobile Communications Research Laboratory. His research interests include THz wireless channel measurements and modeling.



Cheng-Xiang Wang (Fellow, IEEE) received the B.Sc. and M.Eng. degrees in communication and information systems from Shandong University, Jinan, China, in 1997 and 2000, respectively, and the Ph.D. degree in wireless communications from Aalborg University, Aalborg, Denmark, in 2004.

He was a Research Assistant with the Hamburg University of Technology, Hamburg, Germany, from 2000 to 2001, a Visiting Researcher with Siemens AG Mobile Phones, Munich, Germany, in 2004, and a Research Fellow with the University of Agder, Grimstad, Norway, from 2001 to 2005. Since 2005, he has been with Heriot-Watt University, Edinburgh, U.K., where he was promoted to a Professor in 2011. In 2018, he joined National Mobile Communications Research Laboratory, Southeast University, Nanjing, China, as a Professor. He is also a part-time Professor with Purple Mountain Laboratories, Nanjing, China. He has authored four books, one book chapter, and more than 430 papers in refereed journals and conference proceedings, including 25 ESI Highly Cited Papers. He has also delivered 22 Invited Keynote Speeches/Talks and nine Tutorials in international conferences. His current research interests include wireless channel measurements and modeling, 6G wireless communication networks, and applying artificial intelligence to wireless networks.

Prof. Wang is a Member of the Academia Europaea (The Academy of Europe), a Fellow of IET and China Institute of Communication (CIC), an IEEE Communications Society Distinguished Lecturer in 2019 and 2020, and a Highly-Cited Researcher recognized by Clarivate Analytics in 2017-2020. He is currently an Executive Editorial Committee Member of the IEEE TRANSACTIONS ON WIRELESS COMMUNICATIONS. He was the Editor of nine international journals, including IEEE TRANSACTIONS ON WIRELESS COMMUNICATIONS from 2007 to 2009, IEEE TRANSACTIONS ON VEHICULAR TECHNOLOGY from 2011 to 2017, and IEEE TRANSACTIONS ON COMMUNICATIONS from 2015 to 2017. He was a Guest Editor of the IEEE JOURNAL ON SELECTED AREAS IN COMMUNICATIONS, Special Issue on Vehicular Communications and Networks (Lead Guest Editor), Special Issue on Spectrum and Energy Efficient Design of Wireless Communication Networks, and Special Issue on Airborne Communication Networks. He was also a Guest Editor of the IEEE TRANSACTIONS ON BIG DATA, Special Issue on Wireless Big Data, and is a Guest Editor of the IEEE TRANSACTIONS ON COGNITIVE COMMUNICATIONS AND NETWORKING, Special Issue on Intelligent Resource Management for 5G and Beyond. He has served as a TPC Member, a TPC Chair, and a General Chair for more than 80 international conferences. He was the recipient of twelve best paper awards from IEEE GLOBECOM 2010, IEEE ICCT 2011, ITST 2012, IEEE VTC 2013-Spring, IWCMC 2015, IWCMC 2016, IEEE/CIC ICC 2016, WPMC 2016, WCC 2019, IWCMC 2020 and WCSP 2020. Also, he was the recipient of 2020 & 2021 AI 2000 Most Influential Scholar Award Honourable Mention in recognition of his outstanding and vibrant contributions in the field of Internet of Things.



Jie Huang (Member, IEEE) received the B.E. degree in information engineering from Xidian University, Xi'an, China, in 2013 and the Ph.D. degree in communication and information systems from Shandong University, Jinan, China, in 2018.

From October 2018 to October 2020, he was a Postdoctoral Research Associate with National Mobile Communications Research Laboratory, Southeast University, Nanjing, China, supported by the National Postdoctoral Program for Innovative Talents. From January 2019 to February 2020, he was a Postdoctoral Research Associate with Durham University, U.K. He is currently an Associate Professor with National Mobile Communications Research Laboratory, Southeast University, and also a part-time Researcher with Purple Mountain Laboratories, Nanjing, China. He has authored more than 40 papers in refereed journals and conference proceedings, including one ESI Highly Cited Paper. He has also delivered two tutorials in IEEE/CIC ICC 2021 and IEEE PIMRC 2021. His research interests include millimeter wave, THz, massive MIMO, reconfigurable intelligent surface channel measurements and modeling, wireless big data, and 6G wireless communications.

Dr. Huang was the recipient of best paper awards from WPMC 2016 and WCSP 2020.



Haiming Wang (Member, IEEE) was born in 1975. He received the B.S., M.S., and Ph.D. degrees in electrical engineering from Southeast University, Nanjing, China, in 1999, 2002, and 2009, respectively.

In 2002, he joined the School of Information Science and Engineering, Southeast University, Nanjing, China, and is currently a Distinguished Professor. He is also a part-time Professor with the Purple Mountain Laboratories, Nanjing, China. He has authored or coauthored more than 50 technical publications in the IEEE TRANSACTIONS ON ANTENNAS AND PROP-

AGATION and other peer-reviewed academic journals. He is also the author or coauthor of more than 70 patents, out of which, 52 patents have been granted. His current research interests include AI-powered antenna and radio frequency technologies (iART), AI-powered channel measurement and modeling technologies (iCHAMM), and integrated communications and sensing (iCAS).

Dr. Wang was awarded twice for contributing to the development of IEEE 802.11aj by the IEEE Standards Association in 2018 and 2020.



Xiqi Gao (Fellow, IEEE) received the Ph.D. degree in electrical engineering from Southeast University, Nanjing, China, in 1997.

In April 1992, he joined the Department of Radio Engineering, Southeast University. Since May 2001, he has been a Professor of information systems and communications. From September 1999 to August 2000, he was a Visiting Scholar with the Massachusetts Institute of Technology, Cambridge, MA, USA, and Boston University, Boston, MA, USA. From August 2007 to July 2008, he visited the Darm-

stadt University of Technology, Darmstadt, Germany, as a Humboldt Scholar. His current research interests include broadband multicarrier communications, MIMO wireless communications, channel estimation and turbo equalization, and multirate signal processing for wireless communications. From 2007 to 2012, he was the Editor for IEEE TRANSACTIONS ON WIRELESS COMMUNICATIONS. From 2009 to 2013, he was the Editor of IEEE TRANSACTIONS ON SIGNAL PROCESSING. From 2015 to 2017, he was the Editor of IEEE TRANSACTIONS ON COMMUNICATIONS.

Dr. Gao was the recipient of Science and Technology awards of the State Education Ministry of China in 1998, 2006, and 2009, the National Technological Invention Award of China in 2011, and the 2011 IEEE Communications Society Stephen O. Rice Prize Paper Award in the field of communication theory.



Xiaohu You (Fellow, IEEE) received the B.S., M.S., and Ph.D. degrees in electrical engineering from the Nanjing Institute of Technology, Nanjing, China, in 1982, 1985, and 1989, respectively. From 1987 to 1989, he was a Lecturer with the Nanjing Institute of Technology. Since 1990, he has been with Southeast University, Nanjing, China, first as an Associate Professor and then as a Professor. His research interests include mobile communications, adaptive signal processing, and artificial neural networks with applications to communications and biomedical engineering.

He contributed more than 40 IEEE journal papers and two books in the areas of adaptive signal processing and neural networks and their applications to communication systems. He was the Premier Foundation Investigator of the China National Science Foundation. From 1999 to 2002, he was the Principal Expert of the C3G Project, responsible for organizing China's 3G mobile communications research and development activities. From 2001 to 2006, he was the Principal Expert of National 863 Future Project. He was the recipient of Excellent Paper Award from the China Institute of Communications in 1987 and the Elite Outstanding Young Teacher Award from Southeast University in 1990, 1991, and 1993. He is currently the Chairman of IEEE Nanjing Section. He was selected as IEEE Fellow in 2012 for his contributions to the development of mobile communications in China.



Yang Hao (Fellow, IEEE) received the Ph.D. degree in computational electromagnetics from the Centre for Communications Research, University of Bristol, Bristol, U.K., in 1998.

He was a Postdoctoral Research Fellow with the School of Electronic, Electrical and Computer Engineering, University of Birmingham, Birmingham, U.K. He is currently a Professor of antennas and electromagnetics with the Antenna Engineering Group, Queen Mary University of London, London, U.K. He developed several fully integrated antenna solutions

based on novel artificial materials to reduce mutual RF interference, weight, cost, and system complexity for security, aerospace, and healthcare, with leading U.K. industries, novel and emergent gradient index materials to reduce mass, footprint, and profile of low frequency and broadband antennas, and also co-developed the first stable active non-Foster metamaterial to enhance usability through small antenna size, high directivity, and tuneable operational frequency. He coined the term body-centric wireless communications, such as, networking among wearable and implantable wireless sensors on the human body. He was the first to characterize and include the human body as a communication medium between on-body sensors using surface and creeping waves. He contributed to the industrial development of the first wireless sensors for healthcare monitoring. He has authored or coauthored more than 140 journal papers, and has co-edited and coauthored the books *Antennas and Radio Propagation for Body-Centric Wireless Communications* (Artech House, 2006, 2012) and *FDTD Modeling of Metamaterials: Theory and Applications* (Artech House, 2008), respectively. His current research interests include computational electromagnetics, microwave metamaterials, graphene and nanomicrowaves, antennas and radio propagation for bodycentric wireless networks, active antennas for millimeter/submillimeter applications and photonic integrated antennas.

Dr. Hao is a Strategic Advisory Board Member of Engineering and Physical Sciences Research Council, where he is committed to championing RF/microwave engineering for reshaping the future of U.K. manufacturing and electronics.